AIAA JOURNAL
Vol. 44, No. 9, September 2006

Supersonic Cavity Flows and Their Control

N. Zhuang,* F. S. Alvi,† M. B. Alkislar,‡ and C. Shih§
Florida A & M University and Florida State University, Tallahassee, Florida 32310

DOI: 10.2514/1.14879

A detailed experimental study of supersonic, Mach 2, flow over a three-dimensional cavity was conducted using shadowgraph visualization, unsteady surface pressure measurements, and particle image velocimetry. Large-scale structures in the cavity shear layer and visible disturbances inside the cavity were clearly observed. A large recirculation zone and high-speed reverse flow was revealed in the cavity. In addition, supersonic microjets were used at the leading edge to suppress flow unsteadiness within the cavity. With a minimal mass flux (blowing coefficient $B_c = 0.0015$), the activation of microjets led to reductions of up to 20 dB in the amplitudes of cavity tones and of more than 9 dB in the overall sound pressure levels. The microjet injection also modified the cavity mixing layer and resulted in a significant reduction in the flow unsteadiness inside the cavity as revealed by the shadowgraphs and the velocity-field measurements.

Introduction and Background

CAVITY flow has been the subject of research since the 1950s [1]. Although geometrically simple, the fluid dynamics in such flows are rather complicated. As such, some of the basic mechanisms governing this flow, such as the feedback loop [2] discussed later, are known; however, much of the flow physics governing cavity behavior remains unclear. This topic has seen renewed interest in recent years due to the ubiquitous presence of cavity-type flows in applications, such as the control of flow over open cargo and weapon bays [3–5], and mixing control and enhancement for supersonic combustion [6,7]. High-speed cavity flow is also an ideal candidate for a benchmark problem for high-fidelity computations [8] that are attempting to simulate increasingly high Re number flows [9]. Consequently, recent studies that are mainly experimental in nature have provided valuable data primarily in the form of pressure measurements and flow visualizations, which can be used for the validation of such simulations [10].

Cavity Flows: A Brief Review

The feedback mechanism, first discussed by Krishnamurty [1] in the context of cavity flows, has been elegantly described by Rossiter [2] and is believed to be the reason of flow-induced resonance within the cavity. As the shear layer separates from the leading edge of the cavity, it starts to roll up into large-scale vortical structures due to the Kelvin–Helmholtz instability. When these structures impinge on the trailing edge of the cavity, acoustic waves are generated. These waves propagate to the leading edge within the cavity, because the free-stream flow is supersonic, to further excite the shear layer. This completes the feedback loop. Under certain conditions, when the frequency and the phase of the acoustic waves match those of the shear layer instabilities, resonance is achieved producing significant unsteady hydrodynamic and acoustic loads on the nearby surfaces. The resonance can be so intense that it can lead to significant structural fatigue in open weapon bays and landing gears, in the context of cavity flows.

Among the most distinguishing visual features of cavity flow are the waves outside the cavity that are generated by the large-scale structures in the cavity shear layer. These structures grow very rapidly due to the resonance in the cavity as a result of the flow-acoustic coupling. Krishnamurty [1] was perhaps the first to provide clear visual evidence of such waves where he observed a series of waves being swept downstream by the free-stream flow. Subsequently, Heller and Bliss [11] used water table simulation to observe wave in and outside a 2-D cavity and more recently, Heller and Delfs [12] used schlieren photography to observe waves outside a 3-D cavity. Heller and Delfs classified the waves into four categories as follows: Type 1: the upstream propagating waves above the cavity, due to the disturbances traveling upstream within the cavity. Type 2: the compression and expansion waves which occur intermittently at the leading edge. Type 3: the quasi-steady external bow shocks at the trailing edge due to the impingement of the cavity shear layer. And type 4: the weak compression waves, in the vicinity of the trailing edge. In a subsequent study, Zhang et al. [13] observed shock waves generated by large-scale structures in the shear layer of a 2-D cavity. They classified as "type 3 waves" per their nomenclature. Zhang et al. determined that the angles of these "shock" waves correspond to a Mach angle where the Mach number is essentially the difference between the free-stream Mach number and the convective Mach number of the large-scale structures. For further details regarding the nomenclature, the interested reader is referred to these papers.

In addition to flow visualizations, more quantitative measurements have been obtained for cavity flow where a large number of these studies consist of mean and unsteady surface pressure measurements. Among these some are more recent and notable: Bauer and Dix [14] conducted detailed surface pressure measurements of supersonic cavity flows over a Mach number range of 0.6–5.04; Cattafesta et al. [4] and Kegerise et al. [15] obtained fluctuating surface pressure measurements for low- to high-subsonic cavity flows with the goal of implementing active closed-loop control (more on that later). Similarly, Ukeiley and coworkers [16,17] have examined the unsteady wall pressures to better understand the cavity dynamics and subsequently to control its behavior [10]. These studies confirm the presence of high dynamic pressure loads inside the cavity where the fluctuating pressure spectra are dominated by discrete frequencies, or cavity tones. Furthermore, the results how that the frequencies of these modes are fairly accurately predicted by the well-known Rossiter's model.

More limited attempts have been made to characterize the flow field properties for high-speed cavity flows. Ünalmis et al. [18] measured the dynamic pressure in a Mach 5 cavity flow, and visualized the cavity shear structures using a double-pulsed planar

Presented as Paper 3101 at the 9th AIAA/CEAS Aeroacoustics Conference and Exhibit, Hilton Head Island, SC, 12–14 May 2003; received 1 December 2004; revision received 9 January 2006; accepted for publication 29 January 2006.

*Graduate Student, Department of Mechanical Engineering.
†Associate Professor, Department of Mechanical Engineering. Member AIAA.
‡Research Associate, Department of Mechanical Engineering; currently Engineer/Scientist, Acoustics and Fluid Mechanics, Boeing Commercial Airplanes, P.O. Box 3707, MC 2H-15, Seattle, WA 98124. Member AIAA.
§Chairman and Professor, Department of Mechanical Engineering, Associate Fellow of AIAA

laser scattering (PLS) technique. In addition, they obtained some particle image velocimetry (PIV) measurements for a very limited field of view. For both the PLS and PIV measurements, images were only obtained above the cavity opening. One of the main findings of their work was the lack of correlation between the cavity acoustics and the dominant structures in the shear layer. Murray and Elliott [19] also examined the behavior of the cavity shear layer for supersonic flows using schlieren and double-pulsed PLS. They found that similar to compressible free shear layers, the structures "in the cavity shear layer" become increasingly three dimensional and smaller in extent with increasing Mach number. In a carefully conducted experimental study, Forestier et al. [20] examined a Mach 0.8, deep cavity ($L/D = 0.42$) using unsteady pressures, high-speed schlieren photography, and laser Doppler velocimetry where the visualizations and the velocity data were obtained in the vicinity of the cavity shear layer. Through conditional analysis of their data, Forestier et al. construct a rather comprehensive model of the flowfield behavior under these conditions. Recently, Ukeiley et al. [17] conducted an experimental study of a Mach 0.2 cavity flow for "shallow" ($L/D \sim 5.2$) and relatively "deep" ($L/D \sim 1.5$) cavities. In addition to unsteady pressure and limited hot-wire data, PIV measurements for these conditions was also obtained. The velocity-field data show the presence of a recirculation bubble for both cavities, although the differences in the detailed behavior between the two were found to be significant. Based on their velocity and pressure correlations, Ukeiley et al. used a quadratic stochastic estimation technique to construct a model of the dynamical behavior of the flowfield. They concluded that the shallow and deep cavities appear to display different modes and that it is difficult to predict these modes based on L/D alone.

In summary, as briefly described above, there have been a number of experiments that have provided much insight into the properties of this flowfield. However, a large majority of these studies consist of unsteady surface pressure measurements, followed by flow visualizations (schlieren and/or shadowgraph). With the exception of a few studies, limited measurements of the velocity field (using LDV, PIV, and/or hot-wire) especially inside the cavity, is available in literature. Furthermore, most of this data is for subsonic cavity flows.

In this paper we describe the results of an experimental study of a Mach 2 cavity flow where we examine the flow properties in some detail using unsteady wall pressures, schlieren and shadowgraph flow visualizations, and PIV. The dynamic pressure measurements allow one to compare these properties in the current experiment with similar measurements made by other investigators (Bauer and Dix [14]). The flow visualizations reveal the presence of a number of waves; some of which have been observed by others [11–13]—though perhaps not with the same level of clarity inside the cavity, whereas some wave features appear to be new, as discussed in some detail later. The velocity-field measurements obtained using PIV for the flow inside, as well as in the vicinity of the cavity, is perhaps one of the more notable contributions of this paper. To our knowledge, very limited detailed velocity-field data for supersonic cavity flows is presently available. In addition, with a few exceptions, most experimental studies published to date have been for two-dimensional cavities; that is, where the cavity spans the entire width of the test section. In the present study, the cavity spans roughly one-third of the tunnel width. The velocity field combined with the flow visualizations and pressure measurements allow us to gain a little better understanding of the overall flow behavior.

Control of Cavity Flows—Past and Present

In the past, numerous control devices have been examined in order to suppress the resonance in the cavity flow. Among the many passive actuators explored, sawtooth spoilers [5], static or oscillating fences [10,21], leading edge ramps [22], and rods [10] have been shown to reduce the amplitudes of cavity tones. However, most of these devices are only effective within a limited range of flow conditions and usually have an associated penalty, such as increased drag. Hence, in more recent studies, active control actuators have been explored for cavity flow control. Vakili and Gauthier [23] reported a significant reduction of the dominant tone by blowing compressed air through a highly perforated plate just upstream of the cavity. Stanek et al. [24] used powered resonance tubes to successfully suppress the flow-induced resonance at the cavity modes, as well as reduce the overall broadband noise level. Cattafesta et al. [4] developed a real-time adaptive piezoelectric flap actuator for a Mach 0.74 flow, which successfully suppressed more than 10 dB at the first mode. However, most these actuators either require a fairly large mass flux [21,23,24] or involve moving parts [4] that may fatigue or lose performance over time, to achieve considerable reduction. Interested readers could refer to recent reviews of active control of cavity flows by Rowley and Williams [25] and Cattafesta et al. [26], and the references therein.

Another focus of the present study is the implementation of an active flow control technique, for effective reduction of the high dynamic loads typically observed in cavity flows. Toward this end, supersonic microjets were explored for the control of this flow. They produce a high momentum flux ratio with a very small mass flux ratio (with respect to the free stream). They are small, robust, and easy to manufacture. Supersonic microjets appear to have a strong potential to effectively disrupt the self-sustained feedback loop. As a few examples, they have been successfully used in controlling the

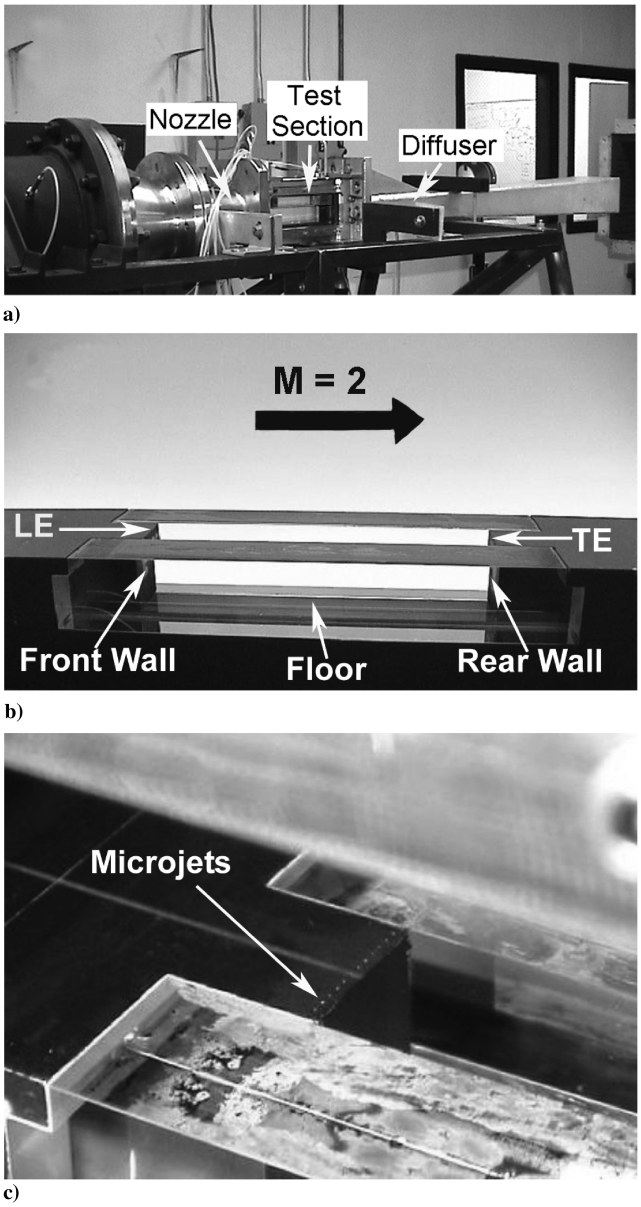

Fig. 1 a) Facility; b) cavity; c) microjets.

feedback loop in high-speed impinging jets [27] and the far-field noise in a supersonic jet [28]. In the present work, an array of microjets was placed very close to the leading edge of the cavity. Significant noise reduction is achieved with a very low mass flux, cavity blowing coefficient [23] $B_c = 0.0015$, with compressed nitrogen. A comparison of the various flow properties, with and without microjet control, not only allows us to evaluate the efficacy of this control approach but may also provide some insight into the reasons behind this approach. In fact the success of this control approach has led to its selection for the control of cavity dynamics in full-scale supersonic sled tests [3].

Experimental Details

Facility and Model

The current study was conducted in the fluid mechanics research laboratory at the Florida A & M University and Florida State University College of Engineering in Tallahassee, Florida. The tunnel is supplied with dry, pressurized air from a bank of high-pressure air tanks. Two high capacity inline heaters are installed to heat the stagnation temperature of the incoming air up to 700 K. A picture of this facility is shown in Fig. 1a, where all four walls of the test section are equipped with optical quality glass windows. In addition, the sidewalls and a replaceable floor of the cavity are fabricated from Schlieren-quality glass to allow for complete optical access for flow visualization and PIV measurements. The test section is 305 mm long, 66 mm wide, and 44 mm high; as shown in Fig. 1a, the cavity is mounted on the ceiling of the test section with the opening facing downward. However, for ease of discussion in the rest of the paper, all images and data have been "flipped" such that the cavity faces upward by convention. In the experiments discussed here, the Mach number is fixed at 2.0. The stagnation pressure was typically maintained at $P_0 = 2.17 \pm 0.02 \times 10^5$ Pa, whereas the stagnation temperature was at $T_0 = 336 \pm 2$ K.

The cavity model, pictured in Fig. 1b, is a 3-D model, occupying the middle one-third width of the test section. The dimensions of the cavity are length $L = 121.9$ mm; depth $D = 23.6$ mm; and width $W = 20.6$ mm, which translates into aspect ratios of $L/D = 5.16$ and $L/W = 5.92$. Because of reflections of the laser sheet by the cavity leading edge, reliable PIV data could not be obtained at and very near the leading edge. Hence, the integral parameters for the separating boundary layer at the cavity leading edge were obtained by linearly extrapolating the momentum thickness from the velocity-field measurements obtained further downstream, from approximately $0.05L$ to $0.4L$, back to the leading edge. Using this approach, the momentum thickness of the boundary layer θ at the cavity leading edge, is estimated to be 0.8 ± 0.2 mm. The Reynolds number is $Re_L = 2.8 \times 10^6$ or $Re_\theta = 1.8 \times 10^4$. The oncoming boundary layer is turbulent.

A row of microjets is used as actuators for controlling the cavity flow, as shown in Fig. 1c. The microjet array simply consists of 12 sonic nozzles, 400 μm in diameter, oriented normal to the surface and incoming free-stream flow. The microjets are evenly spaced with a center-to-center distance of 3.05 mm. The entire row is located 1.5 mm upstream of the cavity leading edge. The microjets are supplied by three small settling chambers that are upstream of the cavity leading edge and under the test-section floor. Each chamber is independent and supplies compressed nitrogen to four microjets, allowing for the spanwise variation of the microjet momentum. However, in this study all three chambers, hence all 12 microjets, are operated at the same pressure.

Experimental Techniques

A conventional z-type shadowgraph system is also used to visualize the flowfield in and above the cavity. A pulsed white light source, with a frequency up to 1000 Hz, is used to illuminate the flow. The duration of each flash is less than 4 μs, which is short enough to freeze most of the turbulent structures and produce instantaneous images of the flow.

Unsteady Pressure Measurements

To measure the mean and unsteady pressure fields, the cavity is instrumented with high-frequency pressure sensors and conventional static pressure ports. They are located along the cavity floor centerplane and at selected spanwise locations. High-frequency pressure sensors used are Kulite model XCE-062-5D transducers, which are flush mounted at the front wall and the cavity floor, and Kulite model XCE-062-100A transducers, which are flushed mounted on the rear wall. The natural resonance frequency for XCE-062-5D is 150 kHz and for XCE-062-100A 380 kHz. The flat frequency responses, according to the manufacturer's specifications, are 20% of its natural frequency. Both transducers have a combined nonlinearity and hysteresis (maximum) of $\pm 0.5\%$. The use of such transducers to measure dynamic wall pressure is well established for low -speed [17] and high-speed cavity flows [10,14,18]. The signals from the Kulite transducers were simultaneously sampled at a rate of 40 kHz and then passed through a low-pass filter with a cutoff frequency of 20 kHz. Two different configurations (A and B) were used for the Kulite locations, as shown in Figs. 2a and 2b, respectively. The actual locations of the Kulite are also given in Table 1. Here the origin of the coordinator is the center of the leading edge as shown in Fig. 2, where X is the streamwise direction, Y is the direction normal to the free stream, and Z is the spanwise direction.

Standard statistical analysis methods are used to obtain various quantities of interest including the spectral density distributions. The unsteady pressure spectra was computed by segmenting each data record into 100 segments with 1 k (1024) points each and an FFT with a frequency resolution of 39.06 Hz was computed for each segment. The 100 FFT's were then ensemble averaged to obtain a statistically reliable estimate of the narrow-band noise spectra. The uncertainty of the unsteady pressure measurement has been estimated as follows: For both measurements (the uncontrolled case and controlled case), the typical error of the measurements using the XCE-062-5D transducers is equivalent to ± 0.5 dB, and the typical error using the XCE-062-100A transducers is ± 1.7 dB, respectively.

PIV Measurements

In addition to the pressure measurement, the PIV technique was also used to measure the velocity field along the cavity centerline. A dual cavity Spectra Physics PIV 400 Nd-Yag pulsed laser with a

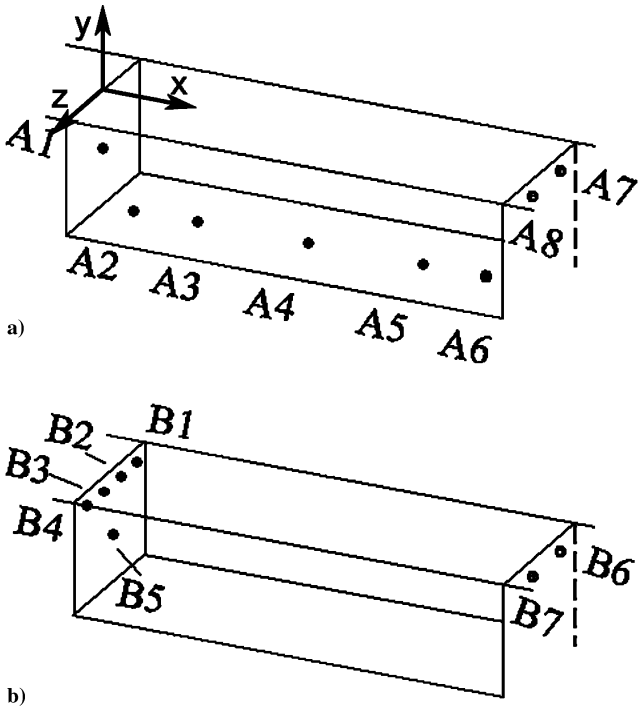

Fig. 2 Pressure sensor locations.

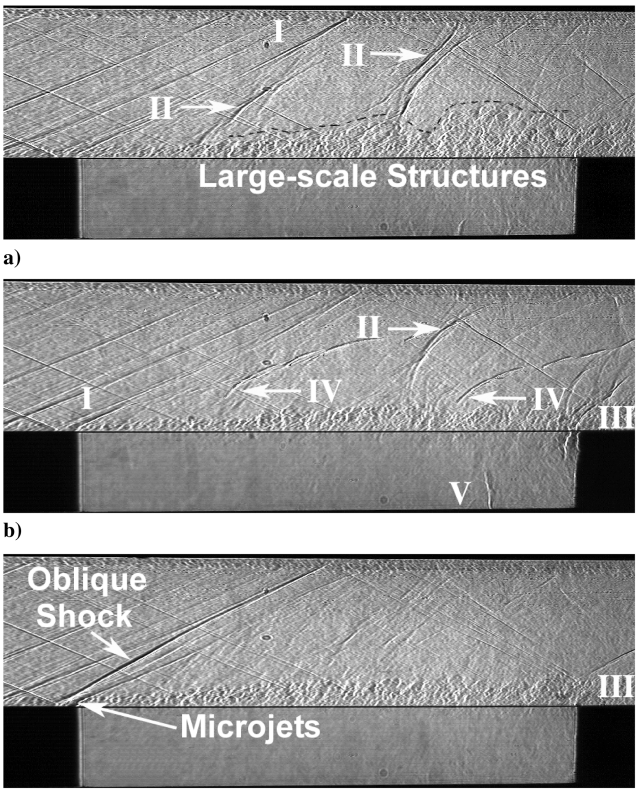

Fig. 3 Instantaneous shadowgraph images, a) and b) baseline cases; c) with microjets control case.

repetition rate of 15 Hz was used to illuminate seed particles in the flow field. The flow in the wind tunnel is seeded with submicron droplets, generated by a modified Wright nebulizer and a water base solution of glycol. The particles are introduced upstream of the settling chamber of the wind tunnel, thus are well mixed with the flow. To measure with a higher spatial resolution, two simultaneously triggered Kodak ES1.0 digital video cameras were used to capture the upstream and downstream halves of the flow field, respectively. Each camera has a resolution of $1008(h) \times 1018(v)$. The flow field is subsequently reconstructed after the processing of the PIV images.

The accuracy of the PIV measurements is determined by many factors, such as the number of samples, turbulence intensity, computation algorithm and most important, particle sizes. A detailed treatment of this subject is outside the scope of this paper, and the reader is referred to the papers by Lourenco et al. [29] and Alkislar [30]. In addition, Alkislar [30,31] contains a comprehensive discussion of the use of PIV in supersonic flows using the same or similar hardware and seeding techniques that are used for the present study. Only a brief discussion is included here. Because the velocity field inside the cavity and the shear layer is not known a priori, one cannot compare the measured values with the expected values. However, in the free stream, the measured velocity is within 2% of the velocity predicted from 1-D gas dynamics under the present tunnel conditions. Nevertheless, certain measurement uncertainties can be estimated using standard statistical analysis methods discussed next.

The velocity-field data shown here were obtained from an ensemble average of 200 or more instantaneous PIV image pairs. As the results discussed later show, the maximum turbulence intensity in the shear layer, u_{rms}/U_∞, measured is 25%. Using the approach outlined by Grant and Owens [32], this results in a relative error of up to 3% in the mean velocity for a 95% confidence level. It also translates to an uncertainty of no more than 10% in the turbulence intensity measurements. The size of the seed particles determine its ability to faithfully track the flow and some particle lag is inherent in any such technique. In the current measurements, we estimate that more than 90% of the particles generated by the seeder are less than 0.5 μm in diameter and the nominal particle diameter is about 0.3 μm [30]. Using the method described by Chung and Troutt [33], the aerodynamic time constant of the particle τ_p for the seed particles is estimated to be 0.4 μs. The dominant frequency in our experiment is 5.5 kHz (based on the measurement of the wall dynamic pressures), which translates to a characteristic time scale for the large-scale structures of $\tau_s \approx 200$ μs, that is, roughly 3 orders of magnitude larger than the aerodynamic response time. An estimate of the "filtering" effect of particle lag shows [34] that under the present conditions, the rms velocities should be accurately captured for velocity fluctuations as high as 50 kHz, which is above the filter cutoff frequency for the dynamic pressure measurements.

One of the most significant effects of particle lag is in areas with high velocity gradients, such as in the vicinity of shock waves. No significant shock waves are present in the baseline cavity flow, except the bow shock near the cavity trailing edge. Only very weak compression waves, essentially Mach waves, are generated at the cavity leading edge and over most of the length of the cavity, for the baseline flow. A weak oblique shock is present when the microjets are activated (to be shown and discussed in the section on Control with Microjets). A comparison of the shock angles obtained from the PIV measurements and the shadowgraphs shows that the shock angles can be measured within 2 to 4 deg from the PIV data. In summary, although particle lag effects are inherent in such measurements, they are minor for most cases examined here. Furthermore, where present, they do not measurably affect the conclusions stated in this study based on the velocity-field measurements.

Results and Discussion

In this section, we first present and discuss the experimental results pertaining to the cavity flow without control, subsequently referred to as the *baseline case*. This is followed by a discussion of the results where microjet control has been applied to the cavity flow, referred to as the *microjet control* cases. For each case, the results are organized in the following sequence: flow visualizations, unsteady surface pressure measurements, and velocity-field data.

Baseline Case (No Control)

Flow Visualization

As mentioned before, the dynamics of the baseline cavity flow are dominated by a feedback loop, comprising the instability waves or shear-layer structures in one leg and the acoustic waves in the return leg. By using the proper flow visualization methods, these structures and wave patterns are made visible, as seen in Fig. 3 which shows a group of instantaneous shadowgraph images for the present cavity flowfield. The flow direction is from left to right. Here Figs. 3a and 3b illustrate the baseline case whereas Fig. 3c shows the microjet control case. Straight oblique waves are visible in the left part of the images in Figs. 3. A measurement of their wave angles demonstrates that these are weak compression waves in that the wave angles are the Mach angle. One of the waves can be traced to the junction of the nozzle and the test section whereas others are due to scratches and imperfections on the tunnel walls. Although every attempt was made to smooth and polish the surfaces and achieve perfect mating of the various tunnel components, such imperfections which generate weak waves are frequently present in most supersonic facilities. A straight oblique shock is seen in Fig. 3c near the cavity leading edge, due to the activation of the microjets. Further discussion of the flow with microjet control is delayed until later in this paper. In summary, the clearly visible oblique "shocks" in Figs. 3a and 3b, discussed so far are relatively weak compression waves, which do not influence the cavity feedback loop in any significant manner (this is further addressed later). Next, we discuss some of the unsteady wave and shear-layer features observed in the flow visualizations.

As the shear layer "flaps" up and down, it generates a type I wave, such as the one indicated in Fig. 3a. It is a compression wave when shear layer flaps up and is an expansion wave when the shear layer

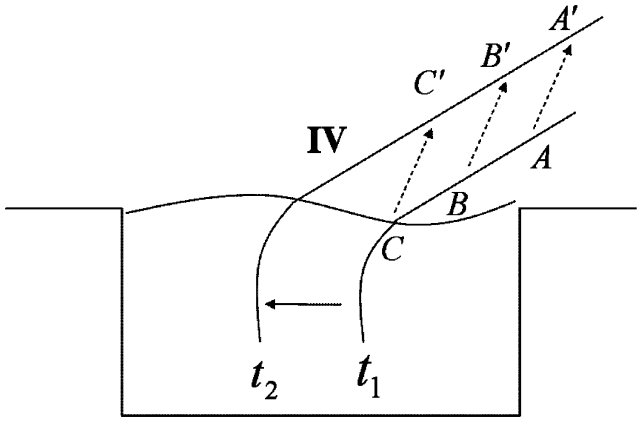

Fig. 4 Wave front of wave (IV) moves toward upstream.

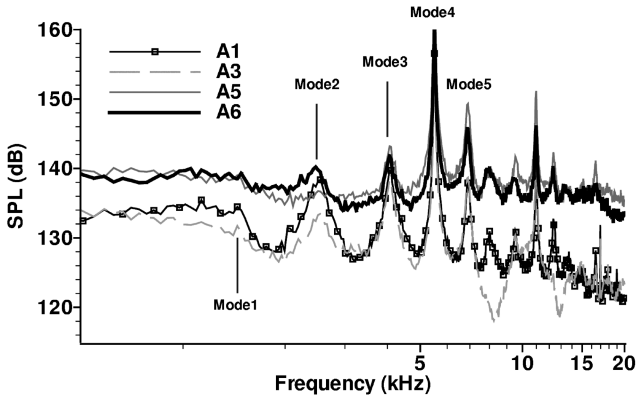

Fig. 5 Pressure spectra at different locations.

flaps down. These waves have been referred to as the "quasi-steady compression shock" by Heller and Bliss [11]. As instability waves in the shear-layer travel further downstream, they rapidly evolve into large-scale structures. Figure 3a shows clearly two such large-scale structures indicated by dashed lines. Two waves, marked as type II waves and shown in Fig. 3a, are trailing these structures and travel across the cavity toward downstream, as shown by the arrows. When the large-scale structures impinge on the trailing edge, bow shocks are formed and acoustic waves are generated. The bow shock is indicated as a type III wave and is visible near the trailing edge in Figs. 3b and 3c. The acoustic waves propagate upstream within the cavity at the local speed of sound, and in doing so they perturb the shear layer over the cavity which generates type IV waves in the free stream. The generation process of a type IV wave is schematically illustrated in Fig. 4. At time t_1, the perturbation of the shear layer due to the acoustic wave generates the wave ABC, a type IV wave above the cavity. At a later time t_2, as the acoustic wave travels upstream inside the cavity, the external type IV wave has propagated upstream to A′, B′, and C′. Because the source of these disturbances is moving upstream inside the cavity, the velocity of this perturbation relative to the free stream is roughly equal to the sum of the free-stream velocity plus the acoustic velocity inside the cavity. Accordingly, the Mach angle of type IV waves will be less than that of type II waves, as seen in Fig. 3b.

The four different types of waves discussed above have been observed in supersonic cavity flows by other investigators [11–13]. However, in the present visualizations, we also clearly see an additional wave feature, marked as a type V wave (Figs. 3a and 3b) that, to the authors' knowledge, has not been observed to date. It is presumably an example of the upstream propagating acoustic wave or perturbation that is generated at the trailing edge by the impact of the shear layer. This type V wave appears at random locations in the visualizations, and is of varying strength (visually) and shape. It is of interest to note that, based on the shadowgraph images, waves of this type are most clearly visible near the cavity floor, and appear to become less visible and perhaps weaker as they approach the shear layer. Consequently, to date we have not explicitly observed type V waves to be connected with type IV waves. These internal cavity waves have rather interesting shapes, where in some cases, a single wave near the cavity floor splits into multiple branches as it approaches the cavity mixing layer. A close examination of Fig. 3a shows the presence of at least two such waves, both of which are much weaker than the type V wave seen in Fig. 3b. The shape, size, and the number of waves inside the cavity can in principal be a function of many parameters including the mode (alternately, the frequency and phase) of the disturbances in the impinging shear layer; the interaction between multiple waves generated by these disturbances and the interaction between upstream and downstream traveling waves; and finally the three-dimensional effects due to the cavity geometry. In addition, their behavior can also be modified by the unsteady flow due to the pulsing, essentially the violent expansion and contraction, of the recirculation region or the bubble that is present inside the cavity (discussed later). The nature and behavior of this feature is intriguing and worthy of further study.

Unsteady Pressures

Large-scale structures in the mixing layer, waves inside the cavity, and the resulting feedback loop all lead to a highly unsteady flow. The spectra of fluctuating pressures confirm this, as shown in Fig. 5. The fluctuating pressures shown here were measured by Kulite flush mounted on the inner surface of the cavity, at different locations according to configuration A (see Fig. 2a and Table 1). To avoid clutter, only spectra from selected Kulites are shown. The presence of discrete, large amplitude peaks, which correspond to the cavity tones, are clearly seen. The cavity tones occur at the same frequency regardless of the transducer location, a feature that is indicative of the global instability, a nature of the feedback loop governing this flow. The multiple peaks at different frequencies are often referred to as different "modes" of the cavity. Using Eq. (1), which is a modified form of Rossiter's model, one can match the tones at various frequencies to different modes, indicated as modes 1, 2, 3 and so on in Fig. 5. Note that mode 1 is not very distinct at all transducer locations. In this equation, f represents the frequencies of the cavity tones; L is the cavity length; m is the mode number, $m = 1, 2, 3, \ldots$; r represents the phase delay between the impact of the large-scale structure on the trailing edge and the generation of the acoustic wave ($0 < r < 1$); M_∞ is the free-stream Mach number; γ is the ratio of specific heat; k is the ratio of the convective velocity of the large-scale structure to the free-stream velocity. By using the frequencies in Fig. 5 and modes in Eq. (1) and assuming r and k are unknowns, one can actually estimate the value of r and k using the least-square method. The method yields values of $r = 0.1$ and $k = 0.6$. Note that the difference in the determined phase delay term r is significantly different than that used in Rossiter's original equation where $r = 0.25$ and $k = 0.57$. However, over the years, researchers have used a range of these values on an ad hoc basis in order to best fit their results. Using phase-locked PIV measurements, the convection velocity of the large-scale structures associated with the dominant tone was measured. These measurements yield a value of

Table 1 Location of Kulites (unit in mm)

	Configure A			Configure B		
	X	*Y*	*Z*	*X*	*Y*	*Z*
1	0	−11.8	0	0	−3.8	−6.9
2	15.2	−23.6	0	0	−3.8	−2.3
3	35.6	−23.6	0	0	−3.8	2.31
4	61.0	−23.6	0	0	−3.8	6.9
5	86.4	−23.6	0	0	−11.8	0
6	106.7	−23.6	0	121.9	−3.8	−3.4
7	121.9	−3.8	−3.4	121.9	−3.8	3.4
8	121.9	−3.8	3.4	——	——	——

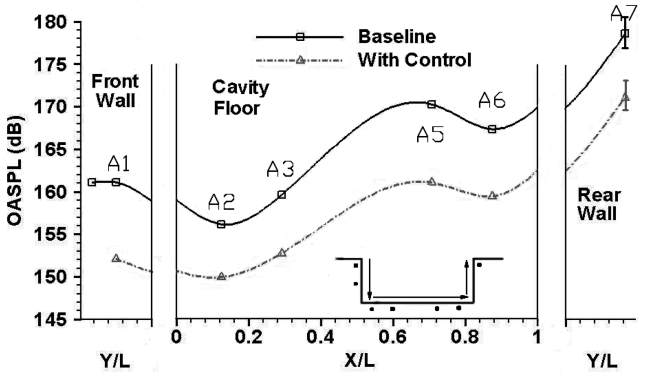

Fig. 6 OASPL reduction along the centerline of the cavity.

$k = 0.58 \sim 0.6$. Given the agreement between the linear fit to the data discussed earlier, and the direct measurement of the convection velocity, we use a value of $k = 0.6$. Note that changing the value of k will not significantly change the Rossiter modes.

$$f = \frac{U}{L}\frac{(m-r)}{\{M_\infty/\sqrt[2]{1+[(\gamma-1)/2]M_\infty^2}\}+1/k} \tag{1}$$

Although the overall spectral features at all locations are very similar, there are subtle differences. Transducers A1 and transducer A2 (whose spectrum was similar to A1 hence not shown here) show very clear peaks at modes 2 and 3. However, at A5 and A6, which are located in the downstream part of the cavity floor, modes 2 and 3 are not as dramatic relative to the local broadband levels. In fact at A5, a discrete tone corresponding to mode 2 is not observed at all. The evolution in the spectral content is expected, because different flow mechanisms come into play as one moves from the cavity leading edge to the trailing edge. For example, in the upstream portion of the cavity, the mixing layer is thin and the primary source of disturbances in that region is acoustic in nature. However, further downstream, the mixing layer structures have grown in size and there are large excursions of the mixing layer into the downstream portion of the cavity, as seen in the shadowgraphs shown in Fig. 3 and also in the velocity-field data to be shown later. Consequently, the unsteady pressures measured in this region are influenced not only by the global unsteadiness of the flow but also by the properties of the highly turbulent cavity mixing layer, which imposes additional scales on the flow dynamics.

Another trend observed in the spectra shown in Fig. 5 is the change in the broadband along the streamwise direction. This trend can be better captured by plotting the overall sound pressure level OASPL [where $\mathrm{OASPL} = 20\log_{10}(P_{\mathrm{rms}}/20\ \mu\mathrm{Pa})$ represents the total energy under the spectra], with respect to transducer locations, as done in Fig. 6. For now concentrating only on the data for the baseline case, that is, flow without control (shown by the solid line and square symbols), this figure reveals that P_{rms} increases in the streamwise direction. The lowest values occur on the front wall, whereas the highest dynamic pressures are measured on the trailing edge surface. In light of the discussion in the preceding paragraphs, where the flow is increasingly influenced by the direct impingement of the cavity mixing layer in the downstream portion, this trend is expected. In this figure, the uncertainty is equal to the size of the symbol, except for the transducer A7 where the uncertainty is indicated by the error bar. The dashed line in Fig. 6 will be discussed in a subsequent section addressing the effect of microjet control on the flow properties.

The temporal properties of the unsteady flowfield were further explored by examining the coherence and phase relationships of the unsteady pressure signals between transducers at different locations in the cavity. The phase lag (angle) [35] is defined as $\theta_{xy}(f) = \tan^{-1}[Q_{xy}(f)/C_{xy}(f)]$, where $Q_{xy}(f)$ is the quadrature spectral density function and $C_{xy}(f)$ is the coincident spectral density function. The coherence function [35] is defined as $\gamma_{xy}(f) = \sqrt{G_{xy}(f)^2/G_{xx}(f)G_{yy}(f)}$, where $G_{xx}(f)$ and $G_{yy}(f)$ are the autospectral density function and $G_{xy}(f)$ is the cross-spectral

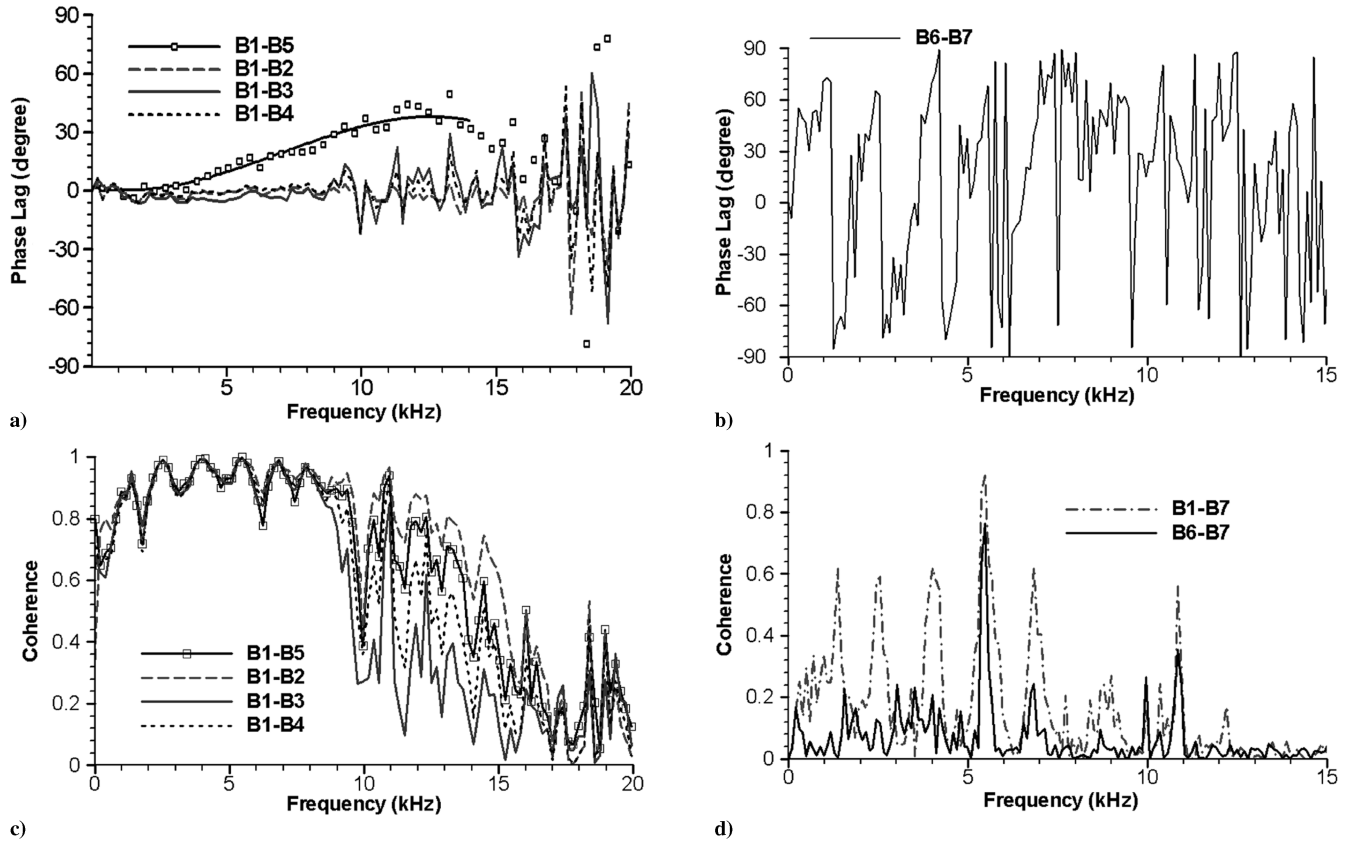

Fig. 7 Phase relation and coherence between transducers signals a) LE phase lags between A1 and A2–A5; b) TE phase lags between A6 and A7; c) LE coherence between A1 and A2–A5; d) TE coherence between A6 and A7.

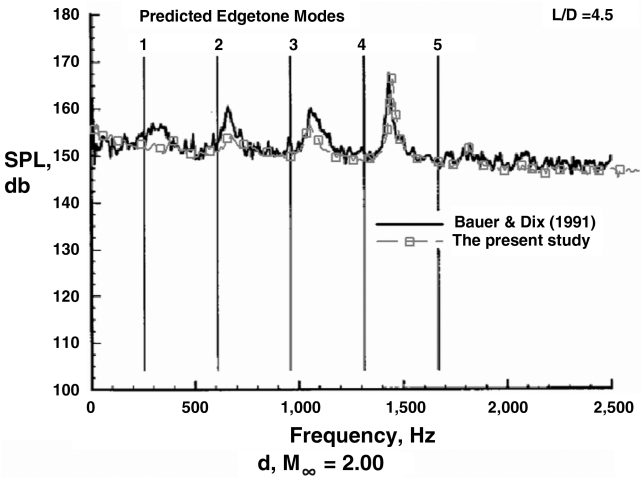

Fig. 8 Comparison with larger scale model test.

density function. Plots showing these properties for transducers in configuration B (see Fig. 2) are shown in Fig. 7. Although not shown here, the spectra of the four transducers along the leading edge, B1 to B4, and the one in the center of front wall, B5, are almost identical and essentially exactly collapse into one spectrum. Naturally, it follows that the differences in the overall dynamic pressures levels, P_{rms} for transducers B1 through B5 are also negligible. Figure 7a shows that the phase lags between leading edge transducers. The phase differences between $B1 \sim B2$, $B1 \sim B3$, and $B1 \sim B4$ are negligible up to about 10 kHz. This suggests that the physical distance in Z direction does not influence the propagation of the disturbances near the leading edge. This in turn implies that the disturbances in this region, which are primarily acoustic in nature, are essentially two-dimensional waves, in the Z direction. In contrast, the phase lag between B1 and B5 gradually increases with frequency. This is likely due to the physical distance in the Y direction between transducers, B1 and B5. If one assumes that the wave speed, hence the time delay from B1 to B5 is fixed, the phase difference should increase linearly with frequency; this is roughly the case, as seen in Fig. 7a. The coherence between the transducers at the front wall remains high, close to unity, at all frequencies up to about 10 kHz, shown in Fig. 7c.

The good agreement between the spectra from all of the transducers, together with the negligible phase differences and high coherence, suggests that cavity flow near the leading edge is dominated by disturbances that are strongly two dimensional and invariant along the spanwise direction. Hence the mixing layer is approximately two dimensional near the leading edge. In contrast to the leading edge, the trends observed at the trailing edge, shown in Figs. 7b and 7d, are distinctly different. The two transducers at the trailing edge, B6 and B7, have comparable spectra (not shown here), but the phase lag between them is almost random. Similarly, the coherence between B6 and B7 is also negligible except at the dominant cavity tones, as one would expect, considering the fact that the flow in this region is dominated by the impingement of the highly turbulent and most likely three-dimensional, cavity mixing layer. This is consistent with the observation by Rockwell and Knisely [36].

The size of the model may raise questions about the reliability and universality of our results with respect to data where larger models are used. Similarly, the presence of the oblique waves may lead one to inquire about their influence on the feedback loop. To address this issue we compared our data with the results obtained by Bauer and Dix [14]. They conducted tests under similar conditions, using a cavity that was roughly 4 times larger in all dimensions. In their study, the flow Mach number is $M = 2$; the cavity length is $L = 18$ in.; the aspect ratios are $L/D = 4.5$ and $L/W = 4.5$. Those parameters are very similar to current study. Using measurements from the transducer at A8 (see Fig. 2) for the present study and data

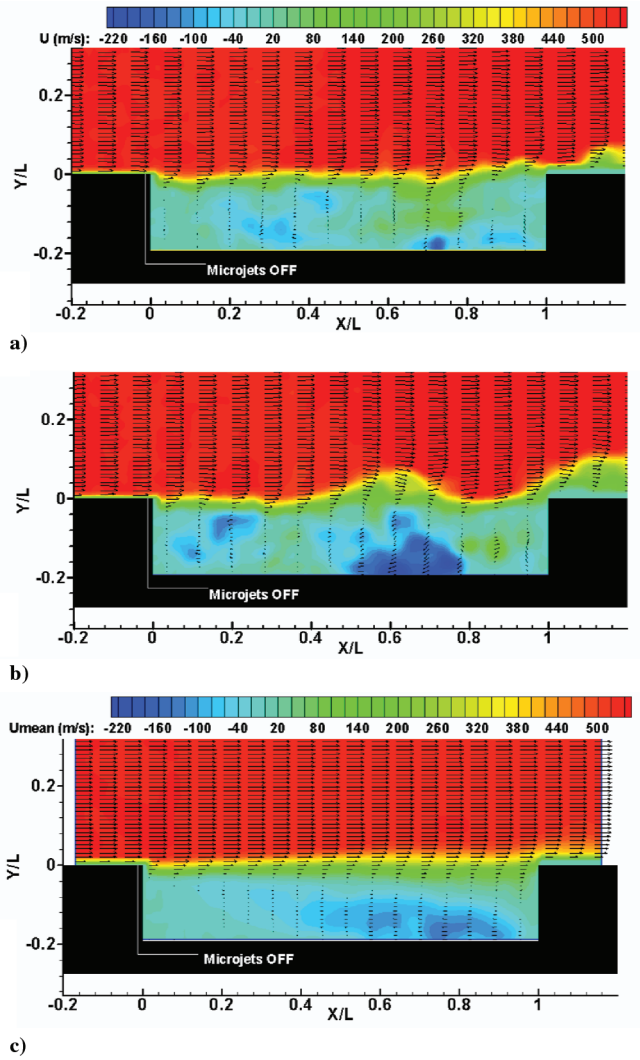

Fig. 9 Instantaneous velocity fields, a) and b); mean velocity-field, c).

from a similarly located transducer K18 (at the center of the trailing edge) from Bauer and Dix's [14] report, a comparison of the unsteady pressure spectra is shown in Fig. 8. Because the frequencies of disturbances in the cavity are inversely proportional to the cavity length, the frequencies from the present results have been scaled (reduced) by a factor of 3.75. Figure 8 shows the original plot digitized from Bauer and Dix's [14] report, with our data superimposed on top (the vertical lines correspond to modes calculated by Bauer and Dix [14]). The excellent agreement between the two experiments is clearly evident. The dominant cavity tone occurs at almost identical frequencies with similar agreement at secondary tones. In addition to the agreement in the frequency content, the overall amplitudes of the tones and the broadband noise characteristics are remarkably similar, this is because the OASPLs are approximately 175 dB in both studies. We note that the stagnation pressure for the Bauer and Dix study were much lower than the present tests, which would normally suggest lower overall noise levels. However, because the OASPLs of the two studies are nearly identical, the noise levels in the incoming boundary layers may be about the same. Information about the upstream conditions is not available in Bauer and Dix [14].

Velocity-Field Measurement

Velocity-field measurements were also obtained using the PIV technique in order to provide more quantitative information regarding this flow. Figures 9a and 9b show two representative instantaneous velocity fields where the velocity vectors have been superimposed on the contours of the streamwise velocity component,

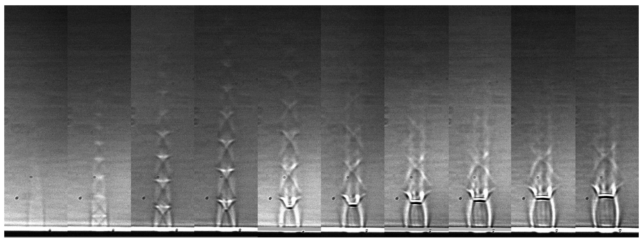

Fig. 10 Microjet actuated in quiescent air with NPR from 2.4 to 14.6.

u. Similar to the shadowgraph images in Fig. 3, the large-scale structures in the mixing layer are clearly evident as undulations in the shear layer. The velocity contours also reveal that very high reverse flow velocities greater than 200 m/s, that is, more than 40% of the free stream value, are present inside the cavity. The maximum reverse flow velocities are primarily confined to the middle and near the bottom half of the cavity. The mean flow properties can be seen in the ensemble-averaged velocity field shown in Fig. 9c. The contours show that although the instantaneous behavior of the mixing layer is rather violent, in a time-averaged sense the mixing layer is relatively straight. The presence of a large recirculation bubble with very high reversed flow velocities—alluded to in the preceding discussion of the wave structures—is evident from this vector/contour plot. This recirculation zone and the accompanying higher reverse flow velocities are confined to the downstream half of the cavity with very low reverse flow velocities in the upstream part of the cavity. This further explains the relatively lower dynamic pressures measured in the upstream portion of the cavity and confirms that the disturbances near the upstream portion of the cavity are primarily acoustic in nature. It is worth noting that the presence of very high reverse velocity regions over a significant portion of the flowfield may result in a countercurrent shear layer, where the high reverse velocity ratio can lead to an absolutely unstable shear layer and a globally unstable flow [37]. In general, a globally unstable flowfield leads to more unsteadiness where the turbulence intensities are higher compared with a convectively unstable flow [8,38]. Whether, this is the case in the present flow cannot be stated unequivocally at present. Having described the behavior of the baseline flow, we now proceed to the discussion of the cavity flow with microjet control.

Microjet Control Case

As described in the introduction section, the actuators used to control the cavity resonance consist of an array of 12, 400 μm diameter sonic micronozzles embedded near the leading edge of the cavity, as shown in Fig. 1c. Compressed nitrogen cylinders are used to supply the gas to the micronozzles in order to form the microjets. A manifold with needle valves is used to precisely control the input stagnation pressure of each microjet to within 6.9 kPa (or 1 psi). As the following results will show, the microjets have been proven to be very effective in disrupting the feedback loop.

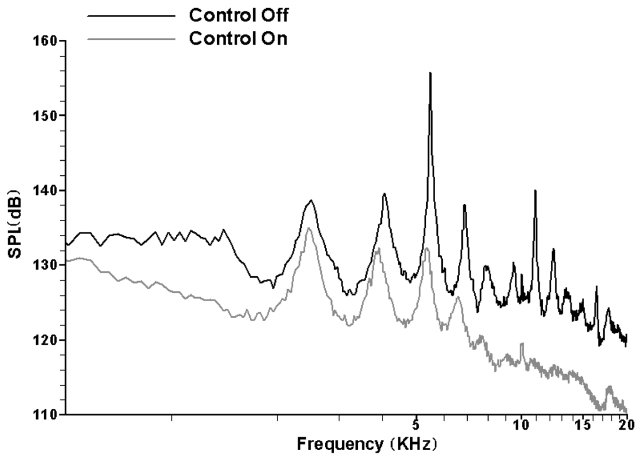

Fig. 11 Spectra comparison between baseline and controlled cases.

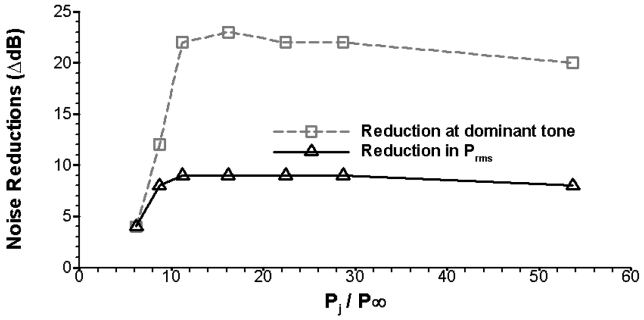

Fig. 12 Control effect vs microjets pressure ratio.

Flow Visualization

Figure 10 shows a series of microschlieren images, with a horizontal knife edge, of flow emerging from one of the microjets used in this study. For the images shown here, proceeding from left to right, the nozzle pressure ratio (NPR, defined as the stagnation pressure divided by the ambient pressure) varies from about 2 to 15. The difference in NPR between each picture is approximately 1.5. As the NPR is increased, both the supersonic core length and the effective diameter increase, a result of the increasing underexpansion ratio of the microjet flow. Also evident is that the microjet flow is clearly supersonic (for the range of pressures shown here), as indicated by the presence of shock cells in the microjet columns. Furthermore, the significant streamwise extent of the supersonic core of the jets, approximately $8 \sim 12$ diameters, or $3 \sim 5$ mm, is also shown in these schlieren images. It is clear that the behavior of supersonic microjets is, at least to a first order, similar to supersonic jets of larger scales [39]. In Fig. 3c, the microjets are operating at an NPR of approximately 11. At this operating pressure, the penetration depth of the microjets in a Mach 2 free-stream flow is estimated to be close to 1 mm, using the jet-in-crossflow correlation proposed by Papamoschou [40]. This penetration depth is of the same order as the boundary layer momentum thickness at this location. A good illustration of a supersonic jet in a supersonic cross flow can be found in Billig's work [41].

The visual effect of the microjets on the flow can also be seen in the shadowgraph of Fig. 3c. When they are activated, an oblique shock is generated just upstream of the microjets. A visual examination of a series of images similar to Fig. 3c reveals that the activation of the microjets leads to a significant reduction in the flow unsteadiness. Most of the wave patterns discussed in the flow visualization section of the baseline case, associated with the highly unsteady behavior of the baseline cavity flow, have either completely disappeared or are rarely seen. These include type I wave, due to the "flapping" of the shear layer, type II waves generated by the large-scale structures in this shear layer, and type IV and V waves due to the strong disturbances inside the cavity. With microjet control only type III waves are still present, although at a weaker strength. Because the presence of these waves, especially those of type V, is an indication of the flow unsteadiness within and in the vicinity of the cavity. Their elimination/significant attenuation suggests that the feedback loop is significantly disrupted.

Unsteady Pressures

The visual reduction in the flow unsteadiness is accompanied by a dramatic reduction of the dynamic pressures inside the cavity. Figure 11 shows a comparison of the pressure spectra, with and without control, for the transducer A1 located at the leading edge. A comparison of the bold line (no control) to the gray line, with microjets control at NPR = 11, shows that the dominant cavity tone is suppressed by 23 dB, whereas the secondary tones are reduced by 5 dB or more. As a result, the magnitude of the previously dominant tone becomes comparable to the secondary tones. Notably, the reduction in the tonal amplitudes is accompanied by a significant reduction in the broadband noise levels as well. For the case shown in Fig. 11, the effect of control translates to a 9 dB reduction in the aggregate unsteady pressure levels P_{rms}. Similar to those shown in

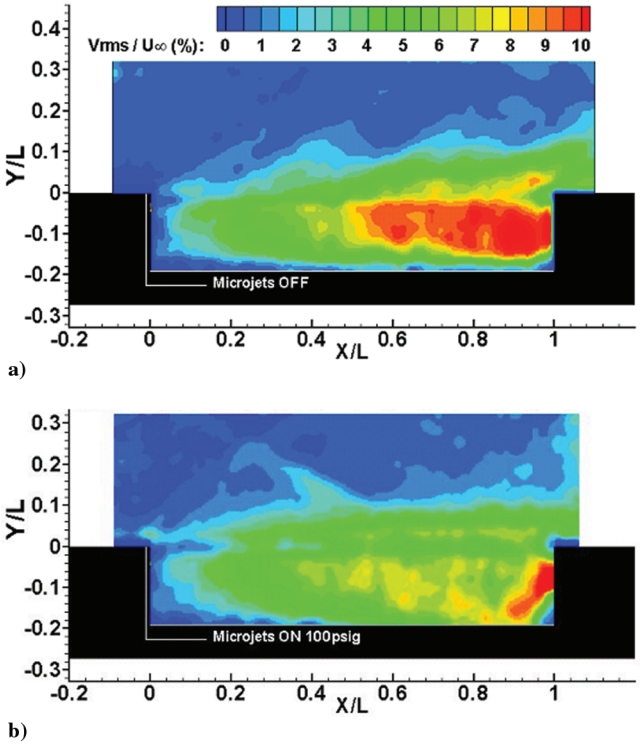

Fig. 13 Comparison of v_{rms} a) baseline; b) with microjets control.

Fig. 11, the effectiveness of microjet control is global, that is, reductions in tonal amplitudes and the broadband levels are observed everywhere in the cavity. The reduction in the overall unsteady pressure levels as a function of location can be seen in Fig. 6 by comparing the dotted line (representing flow with control) with the solid line (representing flow without control).

Although the control data shown so far correspond to the microjets operating at a relatively low NPR, the efficacy of control was examined over a large range of microjet pressures, from NPR = 6 to 54. The effect of microjet pressure on the reduction in the P_{rms} and the amplitude of the dominant cavity tone is summarized in Fig. 12. Uncertainty of the this measurement is equal to the size of the symbols. As seen in this plot, control effectiveness dramatically increases with microjet pressure, up to about NPR = 11. From a noise reduction perspective, this is the optimal control parameter for this configuration. Because beyond this point, saturation occurs and no additional reduction can be achieved. In fact, when the control pressure is increased to NPR = 50, control effectiveness actually decreases. Although data from only one transducer location is shown here, the effect of control is similar throughout the cavity.

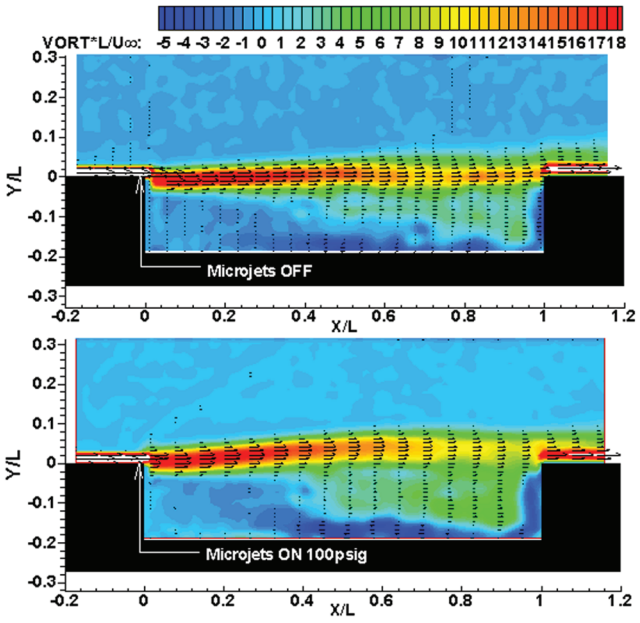

Fig. 14 Vorticity contour comparison.

Earlier in Fig. 11 NPR = 11 was used as an example to represent the case of control with microjets. At this pressure ratio the total mass flux through the 12 microjets is only 0.001 kg/s. To compare our results with other studies, we define the cavity mass blowing coefficient B_c according to Vakili and Gauthier [23], where $B_c = \rho_w V_w A_{inj}/\rho_\infty V_\infty A_{cavity}$ and $A_{cavity} = L_{cavity} W_{cavity}$. Then for the present control technique, the cavity mass blowing coefficient is $B_c = 0.15\%$, when the microjets are operating at 30 psig or NPR = 11. The low mass flux is an extremely important and attractive feature of the present control approach. Compared with other control techniques, the current approach achieves significant reductions in the flow unsteadiness with minimal mass flow. For example, Vakili and Gauthier [23] used at least $B_c = 4\%$ to effectively control the cavity resonance. Similarly the power resonant tubes used by Stanek et al. [24] required $B_c = 1.6\%$ to achieve efficient control. The need for very low mass flux implies that this control technique can in principal be implemented on an aircraft system with a minimal adverse impact on the performance of the aircraft.

Velocity-Field Measurement

In this section we present the effect of microjet control on the velocity field obtained using PIV. Most of the PIV measurements for control cases so far have been obtained for microjets operating at 100 psig or about NPR = 30, as this was the condition first examined using PIV. The reduction in the unsteady pressure levels is concomitant with a reduction in the rms intensities in the velocity field. Figure 13 shows contour plots of v_{rms}, the rms intensity of vertical component of the velocity, where Fig. 13a corresponds to the baseline case and Fig. 13b to the case with microjet control. As seen in Fig. 13a, rms intensities as high as 10% of the free-stream velocity are measured inside the baseline cavity. This is consistent with the instantaneous velocity-field data, shown in Figs. 9a and 9b, where the presence of large unsteady structures inside the cavity are clearly visible. An examination of a series of such instantaneous velocity fields shows large variations in the instantaneous velocities due to such structures resulting in high rms intensities. Upon comparing the rms value of the vertical velocity component, v_{rms} contours for the no control case (Fig. 13a) to the microjet controlled case (Fig. 13b), it becomes evident that not only is there a dramatic reduction in the magnitude of the fluctuating velocities, but the extent of the region where this occurs in the downstream portion of the cavity is also significantly reduced.

Ensemble-averaged vorticity contours of the baseline flow and the flow with control are shown in Figs. 14a and 14b, respectively, where the lengths of the vectors represent the magnitude of the vorticity at that location. It is clear that the center of the mixing layer has been displaced away from the cavity with activation of the microjets. In addition, it appears that the microjets and the oblique shock generated by the microjets cause the free stream flow to deflect from the cavity trailing edge and thicken the mixing layer. The thickening of the shear layer due to control is reflected by the change in the momentum thickness θ, which increased from $\theta/L \sim 0.65\%$ to $\theta/L \sim 1.3\%$ when the microjets are activated at NPR $\approx$ 29. Thicker shear layers, with more gradual velocity gradients, are in general more stable; hence the local thickening is expected to make the cavity shear layer less susceptible to forcing by perturbations, such as the acoustic waves inside the cavity, thus weakening the feedback loop.

The effect of the shear layer displacement is further illustrated in Fig. 15. Here the mean position of the mixing layer is defined as the point of maximum vorticity. Uncertainty of the measurement is represented by the vertical line through the symbols. Because the mean position of the mixing layer has been displaced away from the cavity trailing edge into the free stream when the microjets were

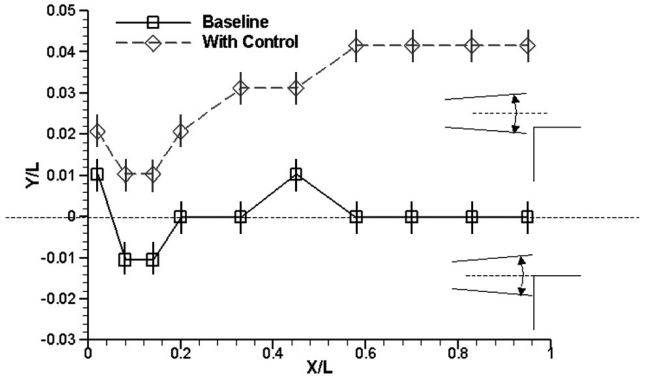

Fig. 15 Comparison of shear layer center corresponding to trailing edge.

activated, it is reasonable to assume that the probability of the large-scale structures impinging directly on the trailing edge is reduced as a result. Because the impingement of the structures on the trailing edge constitutes a critical part of the feedback loop, a reduction in the frequency of this event will also cause the feedback mechanism to be attenuated. Both of the two factors, thickening the initial shear layer and displacing it away from the trailing edge, would in turn lead to a reduction in the unsteadiness of the cavity flow and a reduction in the cavity tones, as observed in the present study.

In addition to the two mechanisms just described, other mechanisms may also weaken the feedback loop. We anticipate that the activation of microjets also disrupts the spatial coherence of the interaction between the acoustic waves and the two-dimensional mixing layer in the region near the leading edge, thereby further attenuating the feedback loop. The microjets are also expected to generate significant streamwise vorticity, which may additionally weaken the feedback loop by the following mechanism: the enhanced entrainment due to the streamwise vorticity tends to diffuse or weaken the velocity gradients in the mixing layer, thus making it more stable, that is, less receptive to perturbation by the acoustic disturbances [42,43].

Summary and Concluding Remarks

An extensive experimental study of Mach 2 flow over a cavity was conducted using methods such as flow visualization, unsteady pressure measurements and PIV. In addition, the efficacy of a flow control technique which utilizes an array of microjets at the cavity leading edge was also examined.

For the baseline case the feedback loop which dominates cavity flows was clearly observed. The cavity modes could be approximately predicted by the modified Rossiter's equation. Very high dynamic pressures were measured throughout the cavity where the fluctuating pressure spectra are dominated by large amplitude discrete cavity tones. A series of wave patterns, triggered by the various phenomena associated with the cavity feedback loop and the large-scale structures in the cavity shear layer, were observed in the shadowgraphs with notable clarity. Although most of these patterns have been observed before, the presence of waves or disturbances inside the cavity were observed for the first time, to our knowledge. We suggest that this disturbance was associated with the upstream propagating acoustic wave that was generated by the impact of the shear layer structures on the cavity trailing edge.

The baseline flow field near the leading edge was found to be approximately two dimensional, where the unsteady pressures are highly correlated across the cavity width. However, the flow becomes highly three dimensional as one proceeds downstream. This was presumably due to the fact that the flow in the upstream portion of the cavity was dominated by acoustic disturbance whereas the downstream portion of the flowfield was increasingly influenced by the highly turbulent shear layer that was highly three dimensional. The high noise level inside the cavity was accompanied by a very unsteady velocity field, as revealed by the PIV measurements. A large recirculation region was observed inside the cavity where the reverse velocities as high as 40% of the free-stream value were measured. Although the presence of a recirculation zone was expected, the magnitude of the reverse flow velocities was not anticipated to be as high. As a result an absolutely unstable shear layer and a globally unstable flow could be generated. Whether this is the case in the present study is not known.

The use of supersonic microjets at the leading edge to suppress the cavity resonance and reduce flow unsteadiness was very successful. With a minimal mass flux, microjet control led to reductions of up to 20 dB in the cavity tones and reductions of more than 9 dB in the overall sound pressure levels. The reduction was global, that was it occurred everywhere in the cavity, as verified by dynamic pressure and velocity-field measurements. PIV results showed the activation of microjets not only reduced the magnitude of the velocity fluctuation but also significantly reduced the region where the high velocity fluctuation occurred. It is suggested that microjet control is effective in reducing the flow unsteadiness because it disrupts the feedback loop in a number of ways. First, the injection of microjets leads to a local thickening of the shear layer near the cavity leading edge, thus decreasing its receptivity to acoustic disturbances traveling upstream from the trailing edge to the leading edge. Second, the microjets disrupt the spatial coherence of the coupling that occurs between the acoustic waves and the instability waves in shear layer near the leading edge. Third, microjets are expected to generate significant streamwise vorticity [42,43] in the cavity shear layer, which can make it thicker and more three-dimensional, factors which adversely affect the feedback loop. Finally, at higher microjet pressures, the shear layer can be somewhat lifted away from the trailing edge. This reduces duration and the magnitude of the impact of the shear layer structures on the trailing edge which in turn reduces the strength of the upstream propagating disturbances. We believe the main reason this technique is so much more efficient than a number of others investigated to date is that it works to attenuate the feedback loop on many different levels as discussed above.

Acknowledgments

This research was in part supported by a DARPA grant (technical monitor, Steven Walker) through The Boeing Company (technical monitor, William Bower). Discussions with A. Krothapalli have been very useful and we thank him for his advice and support. We also would like to express our thanks to Bobby DePriest and Robert Avant for their help in fabricating the facility and model hardware.

References

[1] Krishnamurty, K., "Sound Radiation from Surface Cutouts in High Speed Flow," Ph.D. thesis, California Institute of Technology, 1956.

[2] Rossiter, J., "Wind-Tunnel Experiments on the Flow over Rectangular Cavities at Subsonic and Transonic Speeds," Aeronautical Research Council, Rept. 3438, 1964.

[3] Bower, W. W., Kibens, V., Cary, A., Alvi, F. S., Raman, G., Annaswamy, A., and Malmuth, N., "High-Frequency Excitation Active Flow Control for High-Speed Weapon Release (HIFEX)," AIAA Paper 2004-2513, 2004.

[4] Cattafesta, L., Shukla, D., Garg, S., and Ross, J., "Development of an Adaptive Weapons-Bay Suppression System," AIAA Paper 1999-1901, 1999.

[5] Shaw, L., Clark, R., and Talmadge, D., "F-111 Generic Weapons Bay Acoustic Environment," *Journal of Aircraft*, Vol. 25, No. 2, 1988, pp. 147–153.

[6] Yu, K., and Schadow, K., "Cavity-Actuated Supersonic Mixing and Combustion Control," *Combustion and Flame*, Vol. 99, Nov. 1994, pp. 295–301.

[7] Gruber, M., Baurle, R., Mathur, T., and Hsu, K., "Fundamental Studies of Cavity-Based Flameholder Concepts for Supersonic Combustors," *Journal of Propulsion and Power*, Vol. 17, No. 1, 2001, pp. 146–153.

[8] Rowley, C. W., Colonius, T., and Basu, A. J., "On Self-Sustained Oscillations in Two-Dimensional Compressible Flow over Rectangular Cavities," *Journal of Fluid Mechanics*, Vol. 455, March 2002, pp. 315–346.

[9] Larchevêque, L., Sagaut, P., Lê, T., and Comte, P., "Large-Eddy Simulation of a Compressible Flow in a Three-Dimensional Open

Cavity at High Reynolds Number," *Journal of Fluid Mechanics*, Vol. 516, Oct. 2004, pp. 265–301.
[10] Ukeiley, L. S., Ponton, M. K., Seiner, J. M., and Jansen, B., "Suppression of Pressure Loads in Cavity Flows," *AIAA Journal*, Vol. 42, No. 1, 2004, pp. 70–79.
[11] Heller, H. E., and Bliss, D. B., "Aerodynamically Induced Pressure Oscillations in Cavities—Physical Mechanisms and Suppression Concepts," Air Force Flight Dynamics Laboratory Technical Report No. AFFDL-TR-74-133, Feb. 1975.
[12] Heller, H., and Delfs, J., "Cavity Pressure Oscillations: The Generation Mechanism Visualized," *Journal of Sound and Vibration*, Vol. 196, No. 2, 1996, pp. 248–252.
[13] Zhang, X., Rona, A., and Edwards, J., "An Observation of Pressure Waves Around a Shallow Cavity," *Journal of Sound and Vibration*, Vol. 214, No. 4, 1998, pp. 771–778.
[14] Bauer, R., and Dix, R., "Engineering Model of Unsteady Flow in a Cavity," Arnold Engineering Development Center Technical Report No. AEDCTR- 91-17, Dec. 1991.
[15] Kegerise, M. A., Spina, E. F., Garg, S., and Cattefasta, L.N., "Mode-Switching and Nonlinear Effects In Compressible Flow Over a Cavity," *Physics of Fluids*, Vol. 16, No. 3, 2004, pp. 678–687.
[16] Ukeiley, L. S., Ponton, M. K., Seiner, J. M., and Jansen, B., "Suppression of Pressure Loads in Resonating Cavities Through Blowing," AIAA Paper 2003-0181, 2003.
[17] Ukeiley, L. S., and Murray, N., "Velocity and Surface Pressure Measurements in an Open Cavity," *Experiments in Fluids*, Vol. 38, May 2005, pp. 656–671.
[18] Ünalmis, O., Clemens, N., and Dolling, D., "Experimental Study of Shear-Layer/Acoustics Coupling in Mach 5 Cavity Flow," *AIAA Journal*, Vol. 39, Feb. 2001, pp. 242–252.
[19] Murray, R. C., and Elliott, G. S., "Characteristics of the Compressible Shear Layer over a Cavity," *AIAA Journal*, Vol. 39, No. 5, May 2001, pp. 846–856.
[20] Forestier, N., Jacquin, L., and Geroy, P., "The Mixing Layer over a Deep Cavity at High-Subsonic Speed," *Journal of Fluid Mechanics*, Vol. 475, Jan. 2003, pp. 101–145.
[21] Sarno, R., and Franke, M., "Suppression of Flow-Induced Pressure Oscillations in Cavities," *Journal of Aircraft*, Vol. 31, No. 1, 1994, pp. 90–96.
[22] Zhang, X., Chen, X., Rona, A., and Edwards, J., "Attenuation of Cavity Flow Oscillation Through Leading Edge Flow Control," *Journal of Sound and Vibration*, Vol. 221, No. 1, 1999, pp. 23–47.
[23] Vakili, A., and Gauthier, C., "Control of Cavity Flow by Upstream Mass-Injection," *Journal of Aircraft*, Vol. 31, No. 1, 1994, pp. 169–174.
[24] Stanek, M., Raman, G., Ross, J., Odedra, J., Peto, J., Alvi, F. S., and Kibens, V., "High Frequency Acoustic Suppression—The Role of Mass Flow, the Notion of Superposition, and the Role of Inviscid Instability—A New Model (Part 2)," AIAA Paper 2002-2404, 2002.
[25] Rowley, C. W., and Williams, D. R., "Dynamics and Control of High-Reynolds-Number Flow over Open Cavities," *Annual Review of Fluid Mechanics*, Vol. 38, 2006, pp. 251–276.
[26] Cattafesta, L., Williams, D. R., Rowley, C. W., and Alvi, F. S., "Review of Active Control of Flow-Induced Cavity Resonance," AIAA Paper 2003-3567, 2003.
[27] Alvi, F. S., Elavarasan, R., Shih, C., Garg, G., and Krothapalli, A., "Control of Supersonic Impinging Jet Using Microjets," *AIAA Journal*, Vol. 41, No. 7, July 2003, pp. 1347–1355; also AIAA Paper 2000-2236, 2000.
[28] Krothapalli, A., Greska, B., and Arakeri, V, "High Speed Jet Noise Reduction Using Microjets," AIAA Paper 2002-2450, 2002.
[29] Lourenco, L. M., and Krothapalli, A., "True Resolution PIV: A Mesh-Free Second Order Accurate Algorithm," *Proceedings of the 10th International Conference in Applications of Laser Techniques to Fluid Mechanics*, Instituto Superior Tecnico, Lisbon, Portugal, 2000.
[30] Alkislar, M. B., "Flow Field Measurements in a Screeching Rectangular Jet," Ph.D. thesis, Florida State University, 2001.
[31] Alkislar, M. B., Krothapalli, A., and Lourenco, L. M., "Structure of a Screeching Rectangular Jet: A Stereoscopic Particle Image Velocimetry Study," *Journal of Fluid Mechanics*, Vol. 489, Aug. 2003, pp. 121–154.
[32] Grant, I., and Owens, E. H., "Confidence Interval Estimates in PIV Measurements of Turbulent Flows," *Applied Optics*, Vol. 29, No. 10, 1990, pp. 1400–1402.
[33] Chung, J., and Troutt, T., "Simulation of Particle Dispersion in an Axisymmetric Jet," *Journal of Fluid Mechanics*, Vol. 186, Jan. 1988, pp. 199–222.
[34] Drain, L., *The Laser Doppler Technique*, 1st ed., John Wiley & Sons, Inc., Hoboken, NJ, 1980.
[35] Bendat, J. S., and Piersol, A. G., *Random DATA*, 2nd ed., John Wiley & Sons, Inc., Hoboken, NJ, 1985.
[36] Rockwell, D., and Knisely, C., "Observations of the Three-Dimensional Nature of Unstable Flow Past a Cavity," *Physics of Fluids*, Vol. 23, No. 3, 1980, pp. 425–431.
[37] Alvi, F. S., Krothapalli, A., and Washington, D., "Experimental Study of a Compressible Countercurrent Turbulent Shear Layer," *AIAA Journal*, Vol. 34, No. 4, 1996, pp. 728–735.
[38] Strykowski, P., Krothapalli, A., and Jendoubi, S., "The Effect of Counterflow on the Development of Compressible Shear Layers," *Journal of Fluid Mechanics*, Vol. 308, Feb. 1996, pp. 63–96.
[39] Phalnikar, K. A., Alvi, F. S., and Shih, C., "Behavior of Free and Impinging Supersonic Microjets," AIAA Paper 2002-3047, 2001.
[40] Papamoschou, D., and Hubbard, D., "Visual Observations of Supersonic Transverse Jets," *Experiments in Fluids*, Vol. 14, May 1993, pp. 468–476.
[41] Billig, F., Orth, R., and Lasky, M., "A Unified Analysis of Gaseous Jet Penetration," *AIAA Journal*, Vol. 9, No. 6, 1971, pp. 1048–1058.
[42] Lou, H., Shih, C., and Alvi, F. S., "A PIV Study of Supersonic Impinging Jet," AIAA Paper 2003-3263, 2003.
[43] Lou, H., Alvi, F. S., and Shih, C., "Active and Passive Control of Impinging Jets," *AIAA Journal*, Vol. 44, No. 1, 2006, pp. 58–66.

H. Chelliah
Associate Editor